ACS APPLIED MATERIALS & INTERFACES

www.acsami.org

Research Article

Microgel-Guided MXene Assembly for High-Performance, Low-Solid Content Conductive Inks

Farivash Gholamirad, Monirosadat Sadati, and Nader Taheri-Qazvini*

Cite This: *ACS Appl. Mater. Interfaces* 2025, 17, 4022−4032

Read Online

ACCESS | Metrics & More | Article Recommendations | Supporting Information

ABSTRACT: Rapid evolution of smart devices necessitates high-performance, lightweight materials for effective electromagnetic interference (EMI) shielding. $Ti_3C_2T_x$ MXene nanosheets are promising for such applications, yet the high solid content typically required for 3D-printable MXene inks limits their scalability and cost efficiency. In this study, we present an MXene-based ink with an ultralow solid content (0.1 vol %) and a high water content (up to 98 wt %) enabled by cross-linked poly(acrylic acid) Carbopol microgels. The microgels facilitate a jammed network, creating a percolated structure that allows MXene assembly at minimal concentrations and achieving the lowest reported solid content for MXene inks to date. The MXene/microgel hybrid ink demonstrates superior rheological properties, matching or surpassing existing formulations, and is readily extrudable for 3D printing complex structures and coatings. Following freeze-drying, the printed MXene aerogels exhibit an electrical conductivity of 360 S/m, an EMI shielding efficiency of 57 dB, and a compression modulus of 1750 kPa, all achieved at an ultralow density of 25 mg/cm^3. This work provides a detailed analysis of the MXene/Carbopol ink's structure-processing-performance relationship, highlighting its transformative potential for scalable 3D printing of conductive, EMI shielding materials across diverse applications.

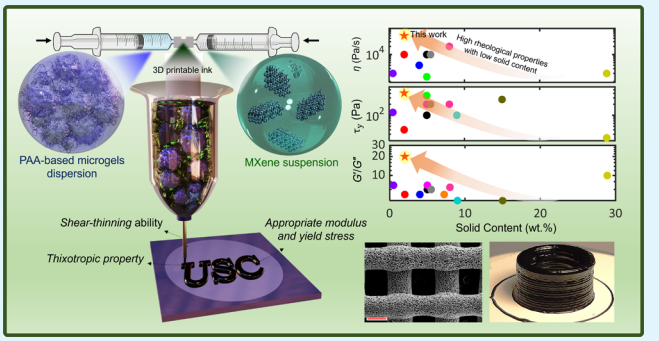

KEYWORDS: *3D printing, EMI shielding, $Ti_3C_2T_x$ MXene, Carbopol, jamming, percolation, rheology*

1. INTRODUCTION

Electromagnetic interference (EMI) shielding is becoming increasingly critical with the rapid advancement and miniaturization of electronic devices.[1,2] As demands for high performance, portability, and miniaturization continue to rise, traditional shielding materials like aluminum and copper are continually optimized to enhance the efficiency; however, their weight, rigidity, and processing limitations hinder their suitability across diverse industries such as aerospace, automotive, military, and telecommunications.[3,4]

In this context, the novel two-dimensional (2D) material $Ti_3C_2T_x$ MXene (where T_x represents OH, O, F, or Cl) has garnered attention due to its unique combination of high electrical conductivity, excellent mechanical properties, and effective EMI shielding capabilities.[5−7] Additionally, MXene's hydrophilic surface functional groups facilitate stable aqueous suspensions, which enables its assembly into solid-state EMI shields.[8−14] Nevertheless, scalable production of MXene-based EMI shields remains a significant challenge as the high solid content typically required for effective conductivity raises production costs and complicates the large-scale manufacturing process.[15]

Extrusion-based 3D printing is emerging as a promising method for the scalable production of MXene-based materials, allowing for high precision, rapid prototyping, and customization of product architecture.[16] However, successful implementation of this technique requires MXene inks with tailored rheological properties, including shear-thinning behavior, thixotropy, yield stress, and storage modulus that can enable stable extrusion and print fidelity.[16] These requirements are difficult to achieve with pure MXene suspensions, which typically necessitate very high MXene concentrations to ensure sufficient structural stability during printing.[17,18] Consequently, achieving the desired performance in MXene-based 3D printing inks often involves trade-offs: while higher MXene content can improve conductivity and stability, it also increases material costs, risk of nozzle clogging, filament roughness, and phase separation during the extrusion process.[17−30]

Various approaches have been explored to overcome these limitations, including the hybridization of MXene with other

Received: November 12, 2024
Revised: December 23, 2024
Accepted: December 25, 2024
Published: January 2, 2025

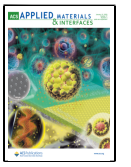

https://doi.org/10.1021/acsami.4c19700
ACS Appl. Mater. Interfaces 2025, 17, 4022−4032

nanomaterials or polymers, which can enhance the ink's rheological properties. For instance, adding conductive polymers such as PEDOT:PSS has shown potential for improving the rheology while preserving the ink's electro-conductive structure.[20,21,24] However, these modifications often require complex processing steps such as the removal of the insulating PSS component through acid treatment to enhance MXene nanosheet contact. These additional processing steps raise production costs, add complexity, and limit the scalability of MXene-based inks for practical applications.[31] Another promising approach involves emulsion-based printing, where MXene nanosheets act as surfactants at the water−oil interface, stabilizing the emulsion and thereby enhancing the rheological characteristics.[32−35] This technique, explored in recent studies, leverages interfacial jamming and can produce ultralightweight, conductive architectures from nanomaterial-based inks by creating stable emulsions. For instance, an emulsion-based ink developed with MXene and graphene oxide has demonstrated excellent stability and porosity, enabling the creation of ultralight architectures with tailored rheological properties optimized for 3D printing.[34,35] Emulsion-based systems also show promise for producing cryogels with high EMI shielding efficiency, even at ultralow densities, due to the numerous internal interfaces that contribute to effective wave dissipation through reflection and absorption mechanisms.[35] Despite these advancements, emulsion-based inks face challenges in maintaining stable and consistent emulsion compositions, particularly at low solid contents, which can affect printability and structural integrity. Furthermore, the requirement for additional surfactants or stabilizers to support emulsion formation can alter the ink's properties and complicate its formulation, limiting its suitability for high-precision applications in 3D printing. Therefore, developing an ink formulation that combines a low solid content with high conductivity and processability for large-scale 3D printing remains an open challenge.

In this work, we explore a MXene ink formulation that leverages the jamming of Carbopol microgels, cross-linked poly(acrylic acid) hydrogel particles, to stabilize MXene nanosheets and form a percolated network at ultralow concentrations. Carbopol microgels, known for their space-filling morphology and gel-like viscoelastic properties, provide a confined structure that enhances the ink's shear-thinning ability, thixotropic behavior, and yield stress at minimal solid content.[36−39] The jamming of these microgels enables a percolated network of MXene nanosheets at ultralow concentrations, reducing the need for high MXene content and providing a practical, cost-effective approach to ink formulation. This approach is designed to achieve two main objectives: (1) reduce the MXene content required for high-performance 3D printing ink and (2) maintain key rheological properties needed for extrusion printing, ensuring structural fidelity without compromising conductivity. By exploring this microgel-assisted assembly technique, we hypothesize that our MXene-based ink will exhibit optimal printability, mechanical stability, and electrical performance, offering a pathway toward the scalable, high-fidelity 3D printing of conductive materials.

2. MATERIALS AND METHODS

2.1. Synthesis of $Ti_3C_2T_x$ MXene. $Ti_3C_2T_x$ MXene is synthesized by selective etching Al atomic layers from the Ti_3AlC_2 MAX precursor (20−200 μm particles, Carbon-Ukraine). Briefly, 1 g of Ti_3AlC_2 powder is added to the etching solution containing 1.5 g of lithium fluoride (99% LiF, Millipore Sigma) in 20 mL of 9 M hydrochloric acid (HCl, Millipore Sigma), and the reaction continues for 28 h at 50 °C. After that, the suspension is washed repeatedly with pure water (18.2 MΩ·cm, 25 °C) until pH ∼ 6. Then, after the separation of the unreacted MAX phase, a delaminated MXene suspension is obtained by centrifugation at 1500 rpm for 30 min. MXene suspension is stored at −70 °C in argon-purged vials for future use.

2.2. Dispersion of Carbopol Microgels. Commercial Carbopol 980 NF (Lubrizol) is used to prepare the inks. Carbopol microgels are prepared by dispersing dried Carbopol powder in pure water using a homogenizer (Fisherbrand 850 Homogenizer) at 25,000 rpm until a homogeneous mixture is obtained. Afterward, 1 M NaOH is gradually added to the Carbopol mixture to increase the swelling ratio of Carbopol particles and obtain a jammed assembly of Carbopol microgels. Consequently, a planetary centrifugal DAC 330-100 SE speed mixer (FlackTek SpeedMixer) is used at 3000 rpm for 3 min to fully homogenize the gel and remove the bubbles.

2.3. Preparation of MXene-Carbopol Gel Inks. The concentration of Carbopol microgels for all recipes is constant at 0.51 wt %, and the concentration of MXene nanosheets for each sample is adjusted. To prepare the inks, Carbopol and MXene dispersions are initially mixed via two interconnected syringes. Then, to ensure the homogeneity of the hybrids, the gel inks are homogenized using the speed mixer (FlackTek SpeedMixer) at 3000 rpm for 3 min.

2.4. 3D Printing of Gel Inks. The gel inks are loaded into a 5 mL syringe and centrifuged at 1500 rpm for 20 s to remove the trapped air bubbles. The Hyrel 3D printer (System 30 M) coupled with an SDS-05 head is used to print 3D objects. The printing process is performed at room temperature using 20−22 gauge blunted needles at a printing speed of 2 to 4 mm/s depending on the geometry of the printed objects.

2.5. Characterizations and Data Analysis. *2.5.1. Rheology.* The rheological behavior of all samples is measured at 25 °C by a Discovery HR-2 (TA Instruments) rheometer, and a solvent trap is used to avoid water evaporation during measurements. For the pristine MXene suspension, a cone and plate geometry (Al, 40 mm, 2.013°, 55 μm truncation gap) is utilized to minimize the effect of the geometry inertia on recorded data. The linear viscoelastic behavior of this sample is collected under oscillating deformations (0.3%, 1 Hz) for 1200 s after being presheared at different shear rates (0−10 1/s) for 30 s. The rheological behavior of gel inks is evaluated using a double cross-hatched parallel-plate geometry (stainless steel, 40 mm, 1 mm gap) to prevent wall slip.

The rheological results are examined by different geometries to ensure the repeatability of the results. All samples are equilibrated for 10 min after loading, and minimum shear is applied during loading. To ensure that the inertial artifacts do not affect the recorded raw data, only data with less than 50° phase shift between the sinusoidal curves of torque and deformation are reported. The oscillation amplitude sweep tests are performed at 1 Hz to examine the linear viscoelastic regime of the gels. The oscillation frequency-sweep tests are conducted at 0.5% strain within the linear viscoelastic regime for all compositions. For all of the oscillation tests, to record the steady-state behavior at each data point, the conditioning and sampling times are both set to 30 s. The flow sweep measurements are performed in cyclic runs from high to low shear rates, and vice versa for each sample. The data points are collected with active steady-state sensing and a sampling period of 30 s. To evaluate the structural recovery, consecutive oscillation time sweeps at the constant frequency of 1 Hz and different strains of 0.5 and 300% are conducted.

2.5.2. Structural Analysis. The morphologies of MXene nanosheets, Carbopol particles, and MXene/Carbopol assemblies are analyzed using FE-SEM (Zeiss Gemini 500) and quantified by ImageJ software. To evaluate the ordering of MXene nanosheets in gel inks and aerogels, X-ray measurements at the transmission mode are performed at the South Carolina SAXS Collaborative (SCSC) using a SAXSLab Ganesha instrument. A Xenocs GeniX, 3D microfocus source is used with a copper target to produce a monochromatic beam with a wavelength of 0.154 nm. A Pilatus 300k detector (Dectris) is used to collect a 2D scattering pattern with the nominal pixel

https://doi.org/10.1021/acsami.4c19700
ACS Appl. Mater. Interfaces 2025, 17, 4022−4032

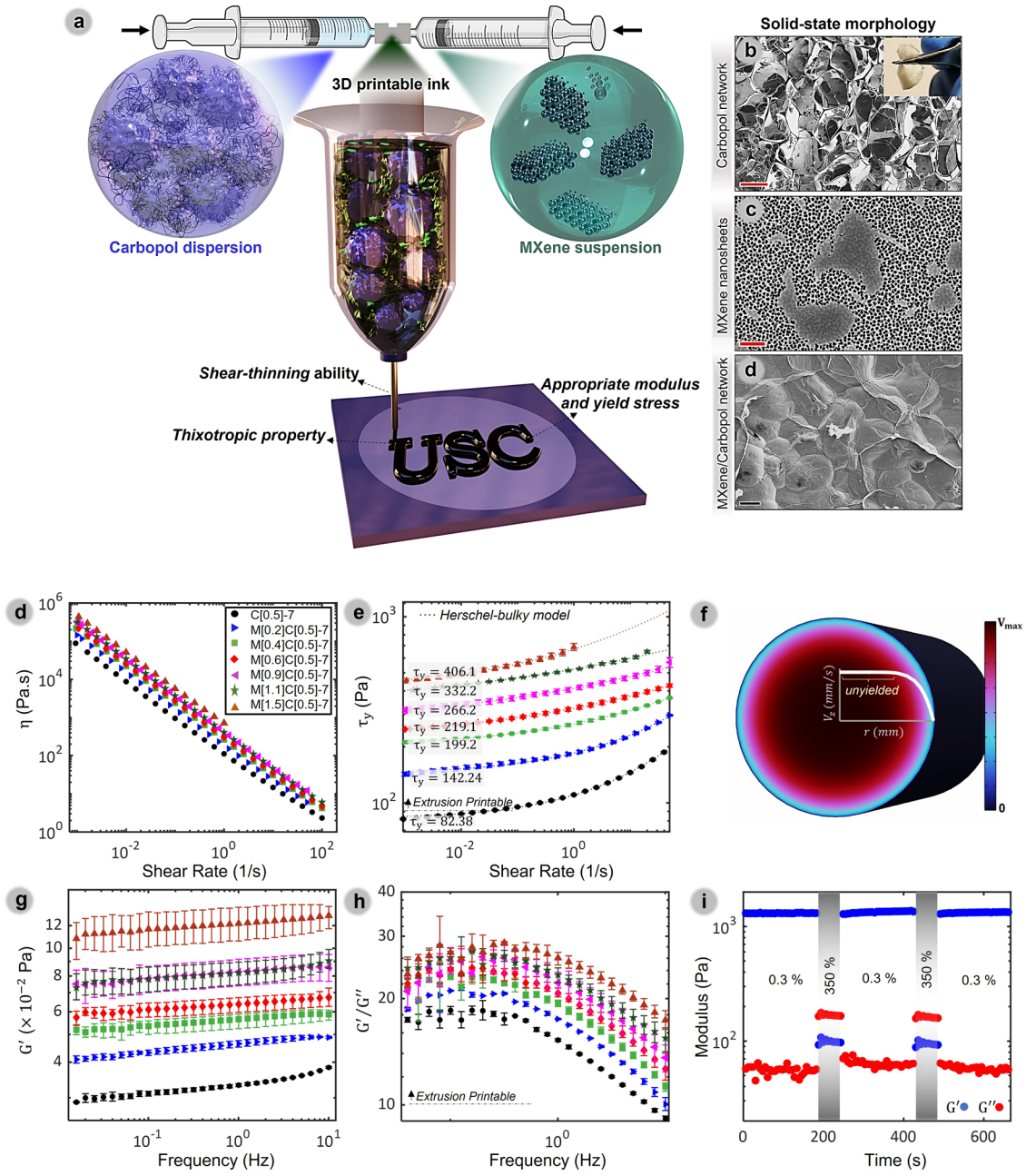

Figure 1. Preparation procedure and rheological properties of MXene/Carbopol gel inks. (a) Schematics illustrating the morphologies of Carbopol dispersion, MXene suspension, and the final ink. SEM images of (b) freeze-dried Carbopol, (c) MXene nanosheets on porous alumina substrate, and (d) freeze-dried MXene/Carbopol hybrid. (d, e) Steady shear rheological behavior of MXene/Carbopol gel inks and (f) fully developed velocity profile of M[1.5]C[0.5]-7 gel ink laminar flow (average velocity of 3 mm/s) in a nozzle (0.6 mm ID) simulated by COMSOL Multiphysics v5.4. (g and h) Oscillation frequency sweep behavior of MXene/Carbopol gel inks at the constant strain of 0.5%. (i) Five-step recovery behavior of M[1.5]C[0.5]-7 gel ink at a constant oscillation frequency of 1 Hz. The scale bars indicate (b) 100 μm, (c) 2 μm, and (d) 50 μm.

dimensions of 172 × 172 mm^2. The 2D images are azimuthally integrated to yield the scattering vector (q) and intensity (I). For the SAXS measurement of gel inks, the samples are encapsulated between two Kapton tapes. Note that no peaks related to the Kapton tape are observed in the "q" range 0.005−0.2 Å^{-1}. The SAXS/WAXS measurements of aerogels are performed on rectangular samples with a thickness of 1.5 mm using standard sample plate holders. SAXS spectra of a gel sample are collected for 90 min, and the SAXS/WAXS data of each aerogel are measured for 60 min. X-ray diffraction patterns are obtained at the speed of 1.2°/min using a powder diffractometer (Rigaku Miniflex II) equipped with a Cu Kα radiation X-ray source.

2.5.3. Composition. To examine the composition of the hybrid, thermogravimetric analysis (TA Instruments, TGA550) is carried out. The sample is heated at 10 °C min^{-1} under an argon atmosphere (130 mL min^{-1}) during the measurement and is vacuum-dried at 80 °C for 24 h before testing.

2.5.4. Electrical Conductivity. The sheet resistance of aerogels is measured by the four-point probe method (Ossila T2001A3).

2.5.5. Mechanical Properties. The mechanical tests are performed using a Discovery HR-2 (TA Instruments) instrument in the compression mode at 25 °C with a linear deformation rate of 0.1 mm/s.

2.5.6. Porosity. The nitrogen adsorption/desorption analysis is performed at 77 K via an ASAP 2020 Plus analyzer. At least, 100 mg

https://doi.org/10.1021/acsami.4c19700
ACS Appl. Mater. Interfaces 2025, 17, 4022−4032

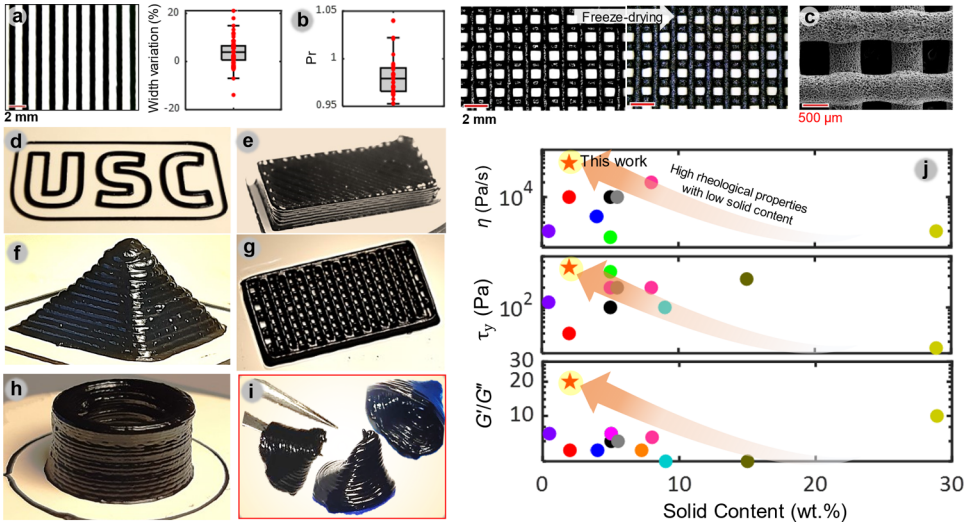

Figure 2. 3D printability of M[1.5]C[0.5]-7 gel ink. (a) Variation in the width of deposited filaments with respect to the nozzle inner diameter (610 μm). (b) Printed grid before and after freeze-drying. (c) SEM image of the printed grid after freeze-drying printed structures. (d) One layer ink coating on the glass substrate, (e) cube 25 × 13 × 3 mm^3, (f) grid 25 × 13 × 2 mm^3, (g) hollow cylinder 17 × 12 × 3 mm^3, and (h) pyramid 15 × 15 × 6 mm^3. (i) Free-standing hydrogel reinforced by hydrogen bonding. (j) Rheological properties of the 3D-printable ink designed in this study and other MXene-based inks reported before.[17,18,20,24,25,27,28,31,32,41−43] The scale bars indicate (a and b) 2 mm and (c) 500 μm.

of the sample is tested, and it is degassed for 72 h at 150 °C under a vacuum before the test.

2.5.7. Particle Size and Zeta Potential. The hydrodynamic size distribution and zeta potential of MXene suspension at a very dilute regime are estimated by the dynamic light scattering technique using a Malvern Instruments Nano ZS instrument.

2.5.8. Optical Imaging. The optical microscopic images are captured under the transmission mode by a ZEISS Axioscope 5 microscope.

2.5.9. EMI Shielding. EMI shielding measurements of aerogels are carried out in the X-band frequency range (8.2−12.4 GHz) using a WR90 waveguide (inner dimension of 22.86 × 10.16 mm^2) connected to the vector network analyzer (ZVA67, Rohde & Schwarz). Aerogels with different compositions and thicknesses are 3D printed (70% filling, 45° filling angle) before being freeze-dried. Each sample is tightly fixed inside the waveguide, and the holder is tightened with screws and clamps to prevent any wave leakage during the test. Three replicates for each sample are prepared, and an average of at least three measurements is reported for each. The "*S*" parameters measured by the vector network analyzer are used to calculate the shielding effectiveness for each sample.

3. RESULTS AND DISCUSSION

Rheological Tailoring and Optimization of Microgel-Guided MXene Ink. Highly stable MXene suspension with average nanosheet sizes between 1 and 3 μm and a zeta potential of −35 mV was prepared through minimally intensive etching and delamination of Ti_3AlC_2 (MAX) compact particles (20−200 μm) (Figure S1, SI). The absence of the characteristic Ti_3AlC_2 peak in the XRD pattern at 39° and the increased *d*-spacing of MXene indicate successful etching with no residual MAX phase remaining in the final product (Figure S2, SI). To develop robust aqueous gel ink formulations compatible with extrusion-based 3D printing, MXene nanosheets were incorporated within a jammed Carbopol microgel matrix (Figure 1a), which creates a confined environment that prevents MXene infiltration due to its lateral micrometer-scale dimensions, as confirmed by SEM (Figure 1b). This confinement facilitates electrical percolation through close interfacial contact, allowing optimal rheological properties without compromising the template's structural integrity. Our hybrid inks, labeled as M[*x*]C[*y*]-*n*, where "*x*" and "*y*" denote the weight percentage of MXene and Carbopol, respectively, and "*n*" represents the pH of the Carbopol dispersion used in ink preparation, exhibit diversity in their formulations (Table S1, SI).

The strong hydrogen bonding between the surface groups of MXene and the carboxylic acid moieties of Carbopol enhances the stability of the composite, maintaining homogeneity and resistance to phase separation, as confirmed by a 30 min centrifugation test at 10,000 rpm with no noticeable stratification (Figure S3, SI). Additionally, freeze-drying showed minimal impact on the ink's internal structure due to the compatibility between MXene sheets and Carbopol particles. In contrast to the collapse observed in Carbopol alone, the MXene/Carbopol hybrid retained its structure, supporting the formation of a solid closed-cell porous network (Figures 1c, entry S4, SI).

The rheological properties of the MXene/Carbopol gel inks were evaluated, with MXene loading varied from 0.2 to 1.5 wt % and Carbopol concentration fixed at an optimal 0.5 wt % to simulate conditions encountered during and after extrusion (Figure 1d−i). The inks demonstrated pronounced shear-thinning behavior (Figure 1d), which is critical for consistent flow through the nozzle during printing. The inks' high viscosity (exceeding 10^5 Pa·s) and yield stress (τ_y) values ranging from 150 to 400 Pa (Figure 1d,e, Table S2, SI) facilitate shape retention postdeposition, a requirement for 3D printing applications. The flow behavior follows the Herschel-Bulkley model ($\tau = \tau_y + k\dot{\gamma}^n$, where τ is the shear stress, k is the consistency index, $\dot{\gamma}$ is the shear rate, and n is the power law index), with n decreasing from 0.362 to 0.24 as the MXene content increases (Table S2, SI). This decreasing trend in the power law index indicates enhanced shear-thinning capability crucial for smooth extrusion. The systematic increase in the yield stress with increasing MXene content correlates with the strengthening of the percolated network structure, as evidenced by amplitude sweep measurements showing an extended linear viscoelastic region (Figure S7, SI). This behavior restricts fluid flow under low stress, preserving

https://doi.org/10.1021/acsami.4c19700
ACS Appl. Mater. Interfaces 2025, 17, 4022−4032

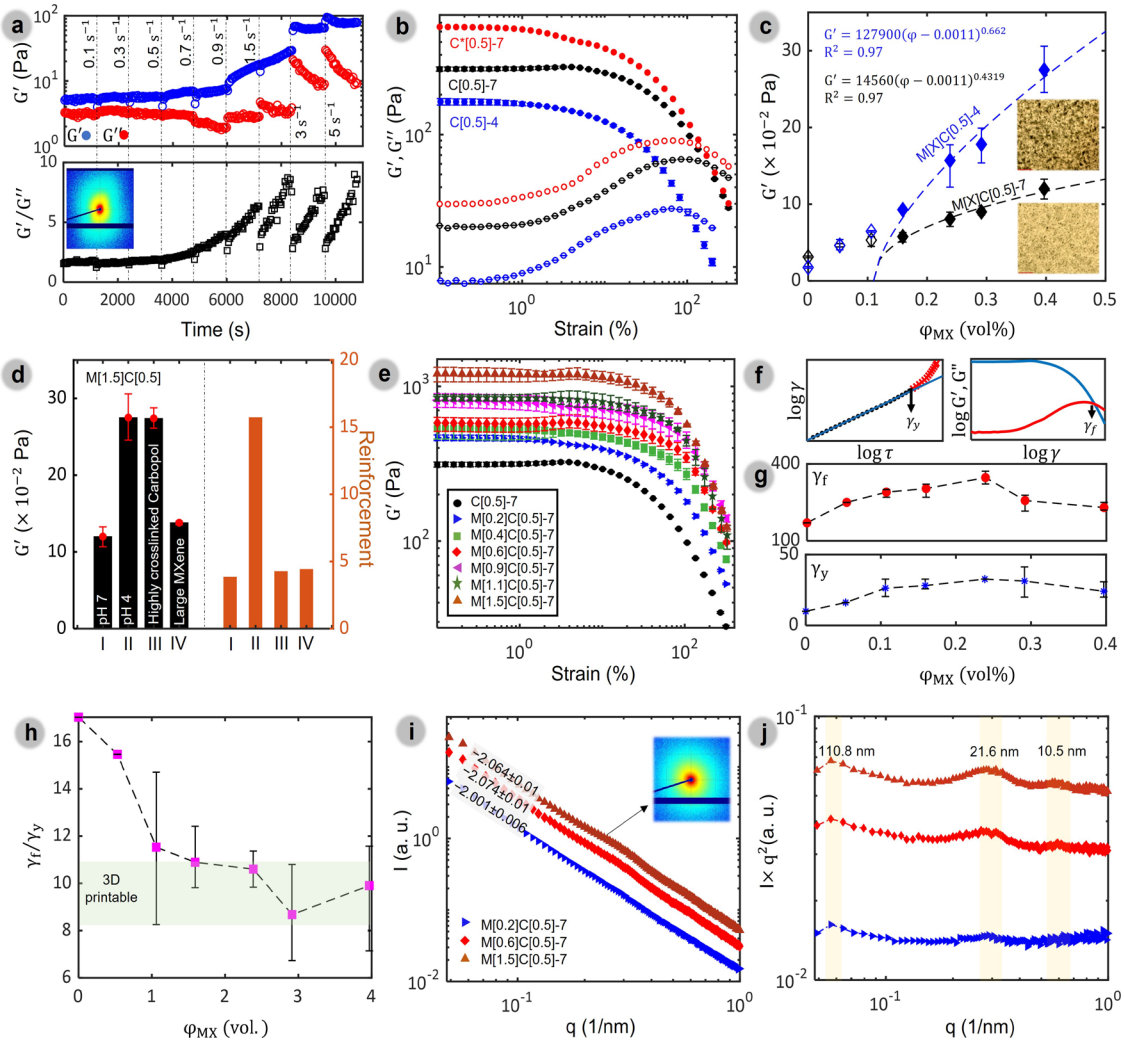

Figure 3. Structural properties of MXene/Carbopol gel inks. (a) Oscillation rheology of pristine MXene ink (1.5 wt %) measured at 0.3% strain amplitude and a frequency of 1 Hz, presheared from 0.1 to 5 s^{-1}. (b) Oscillation strain sweeps of Carbopol dispersions prepared by medium-cross-linked grade at pH 4 (C[0.5]-4) and 7 (C[0.5]-7) or by highly cross-linked grade at pH 7 (C*[0.5]-7) measured at the frequency of 1 Hz. (c) Average storage moduli calculated from the data measured in the linear viscoelastic range at 1 Hz for hybrid inks with the pH of 4 and 7 at different MXene concentrations and their optical microscopic images at 0.4 vol % MXene. (d) Variation in the linear elastic modulus of M[1.5]C[0.5] gel inks and the degree of reinforcement ($G'_{hybrid}/G'_{Carbopol}$) by changing the aggregation states of MXene or Carbopol. (e) Oscillation strain sweeps of hybrid gels measured at 1 Hz. (f) Yield and flow points determination. (g) Change in yield and flow strains by increasing the MXene volume fraction. (h) Change in flow transition index by increasing the MXene volume fraction. (i, j) SAXS scattering intensities as a function of scattering vector q ($q = 2\pi/d$) of MXene/Carbopol gel inks.

structural integrity and enabling rapid recovery of the ink's original modulus after extrusion (Figure 1f).

To further understand the viscoelastic characteristics, we performed oscillatory frequency sweeps under a constant strain of 0.5%, confirming a frequency-independent storage modulus across formulations, indicative of a predominantly solid-like system (Figure 1g). The storage modulus (G') consistently exceeded the loss modulus (G''), with a G'/G'' ratio greater than 5, surpassing the threshold for extrusion printing fidelity. This behavior is further supported by amplitude sweep measurements (Figure S7, SI) showing clear yield points that shift to higher strains with increasing MXene content, indicating an enhanced structural stability. The high G'/G'' ratio signifies that the ink solidifies readily and retains shape immediately upon extrusion (Figure 1h).

Through synergistic interactions between MXene and Carbopol, we achieved optimal rheological properties for 3D printing at an ultralow solid concentration of 2 wt %, where MXene constitutes 75% of the solid mass. The M[1.5]-C[0.5]-7 ink formulation also displayed thixotropic behavior, allowing it to regain its viscoelastic properties instantly after extrusion, a key factor in maintaining the shape fidelity of printed structures (Figure 1i). In a structured five-step recovery test, an initial low strain of 0.3% simulated preextrusion conditions followed by a high strain of 350% to replicate the viscous-dominated regime where G'' exceeds G'. The immediate recovery of storage modulus after high-strain deformation indicates rapid rebuilding of the microgel-MXene network structure, essential for layer-by-layer printing where quick solidification prevents structural collapse. Upon returning to low strain, the storage modulus rapidly recovered, demonstrating the ink's capacity to withstand shear and return to its gel-like state without loss of structural properties.

https://doi.org/10.1021/acsami.4c19700
ACS Appl. Mater. Interfaces 2025, 17, 4022−4032

This rheological profile, achieved at a low MXene content, highlights the efficacy of the microgel-guided assembly in producing a 3D-printable MXene-based ink with remarkable stability and shape retention. Such a formulation reduces material usage and offers the potential for production scalability and cost effectiveness.

3.2. Printability of MXene/Carbopol Gel Inks. The extrusion printability of M[1.5]-C[0.5]-7 ink was evaluated by analyzing the variance in the width of the printed lines based on the nozzle's inner diameter (Figure 2a). The thickness variations of the printed lines are less than 15% compared with the nozzle size, indicating minimal filament spreading. This deviation is significantly below the lowest reported value of 25% measured for Ti_3C_2 MXene-based inks.[20]

The optimal printability of an ink gel should manifest in an extruded filament with well-defined morphology, smooth surface, and consistent width, which in turn results in the construction of regular grids with square holes.[40] The printability characteristic "Pr" ($Pr = \frac{\pi}{4}\cdot\frac{1}{C}$, in which "$C$" denotes hole circularity) of the printed grids should fall within the 0.9−1.1 range for ideal mechanical stability.[40] The Pr values of the printed M[1.5]-C[0.5]-7 grid shown in Figure 2b are approximately 1 ± 0.05, indicating that the 3D printed hydrogel construct presents robust filament morphology and mechanical stability. Moreover, the printed gel ink maintains shape fidelity and integrity with less than 3% dimensional shift after freeze-drying, eliminating the need for additional thermal or chemical treatments (Figure 2b,c).

By exploiting the optimal rheological properties and uniform dispersion of nanosheets in the gel inks, we fabricated various 3D architectures through continuous extrusion printing of M[1.5]-C[0.5]-7 ink (Figure 2d−h). Given the favorable mechanical properties and rapid recovery when shear is absent, the printed gel ink retains geometric features and structural integration upon deposition. Furthermore, by enhancement of hydrogen bonding between components, free-standing hydrogels with excellent shape fidelity were achieved. This was realized by adding 0.9 mg of sodium tetraborate decahydrate and 13 μL of glycerol to 1 mL of MXene/Carbopol hybrid and then allowing the mixture to rest for 24 h in a sealed container at 30 °C (Figure 2i).

The rheological properties of the 3D-printable MXene/Carbopol gel ink with 2 wt % solid content are compared with previously reported 3D printed MXene-based inks (Figure 2j; detailed data in Table S3, SI). Despite having minimal solid content, the ink developed in this study displays rheological properties that are comparable, if not superior, to those reported in other studies. The remarkable properties of the ink are attributed to the percolated network of high-modulus MXene nanosheets throughout the structure, enabled by the space-filling morphology of jammed Carbopol microgels.

3.3. Morphology-Rheology Relationship of MXene/Carbopol Gel Inks. The storage modulus of pristine MXene suspension is largely contingent on the long-range orientation or liquid-crystalline assembly of MXene nanosheets in the system, as explained by Onsager theory.[44] This orientation arises from the repulsive interactions between the nanosheets and is enhanced by applying external deformation to the system or increasing the concentration (Figures 3a and S5, SI). The storage modulus of the isotropic MXene suspension (1.5 wt %) is approximately 5 Pa at the onset of the partial long-range orientation of nanosheets, as illustrated by the anisotropic SAXS diffusive pattern (Figure 3a). As the shear rate increases to 5 s^{-1}, the solid behavior (i.e., G' and G'/G'') progressively improves, with the storage modulus reaching ∼90 Pa (Figure 3a). These observations reveal that the viscoelastic response of the pristine MXene suspension is greatly affected by the shear history, with a recovery time exceeding 1200 s, rendering it unsuitable for 3D printing.

Conversely, the macroelasticity of Carbopol dispersions is governed by the volume fraction and cross-link density of the polymer particles.[33] For the Carbopol 980 NF, characterized by moderate cross-linking density, the highest storage modulus of approximately 300 Pa is achieved for 0.5 wt % dispersion after pH neutralizing (C[0.5]-7 and C[0.5]-4); (Figure 3b). This is attributed to the ionization of carboxylate groups, which triggers the polymer chain uncoiling and microgel swelling due to electrostatic repulsion. Furthermore, as the cross-link density of Carbopol particles increases, the polymer aggregates become larger,[36] and the storage modulus reaches 600 Pa at 0.5 wt %, pH 7 (C*[0.5]-7) (Figure 3b).

Leveraging the close-packed morphology (i.e., jamming) of Carbopol and the high modulus of MXene nanosheets, MXene/Carbopol gels demonstrate synergistic rheological behavior despite the relatively low storage moduli of both the individual MXene suspension and Carbopol dispersion. In accordance with the statistical percolation model,[45] we observe a percolation in the storage modulus (G') at 0.4 wt % (0.1 vol %) of MXene (Figure 3c). This underscores the substantial impact of MXene nanosheets on the rigidity of the MXene/Carbopol solidlike networks due to the multiparticle interactions and friction among closely packed particles. Interestingly, the acidic MXene/Carbopol gel ink, even with the smaller size of Carbopol microgels and their lower storage modulus at pH 4, exhibits a higher storage modulus compared to the neutralized ink, particularly beyond the percolation threshold (Figure 3c). This enhanced reinforcement effect of MXene nanosheets at pH 4 is attributed to nanosheet aggregation, as illustrated by optical microscopic images (Figure 3c). However, such an aggregation is not ideal for 3D printing as it compromises ink homogeneity, potentially causing nozzle clogging and phase separation during the printing process. On the other hand, utilizing Carbopol with a high cross-link density increases the storage modulus of M[1.5]C*[0.5]-7 to 2700 Pa, a significant increase from 1200 Pa achieved with less cross-linked Carbopol (Figure 3d).

The 3D printability of pristine MXene inks is typically influenced by the aspect ratio of MXene nanosheets and the ink concentration.[46] However, the production of highly concentrated suspension (>5 wt %) containing large, few-layered MXene nanosheets for 3D printing poses considerable challenges and demands substantial time.[47] Intriguingly, altering the lateral sizes of MXene does not significantly impact the mechanical properties of MXene/Carbopol gel inks, enhancing the feasibility of this system for large-scale 3D printing of MXene products (Figures 3d and S6, SI).

To distinguish the individual effects of MXene and Carbopol morphologies on the mechanical properties of the gel inks, the reinforcement degree is calculated by normalizing the storage modulus of the gel inks to the respective values for the pristine Carbopol dispersions (Figure 3d). Results suggest that for similar compositions, the aggregation states of both MXene and Carbopol particles profoundly influence the storage modulus of the gel ink. Later sections explore how these parameters impact the solid-state properties of MXene/

https://doi.org/10.1021/acsami.4c19700
ACS Appl. Mater. Interfaces 2025, 17, 4022−4032

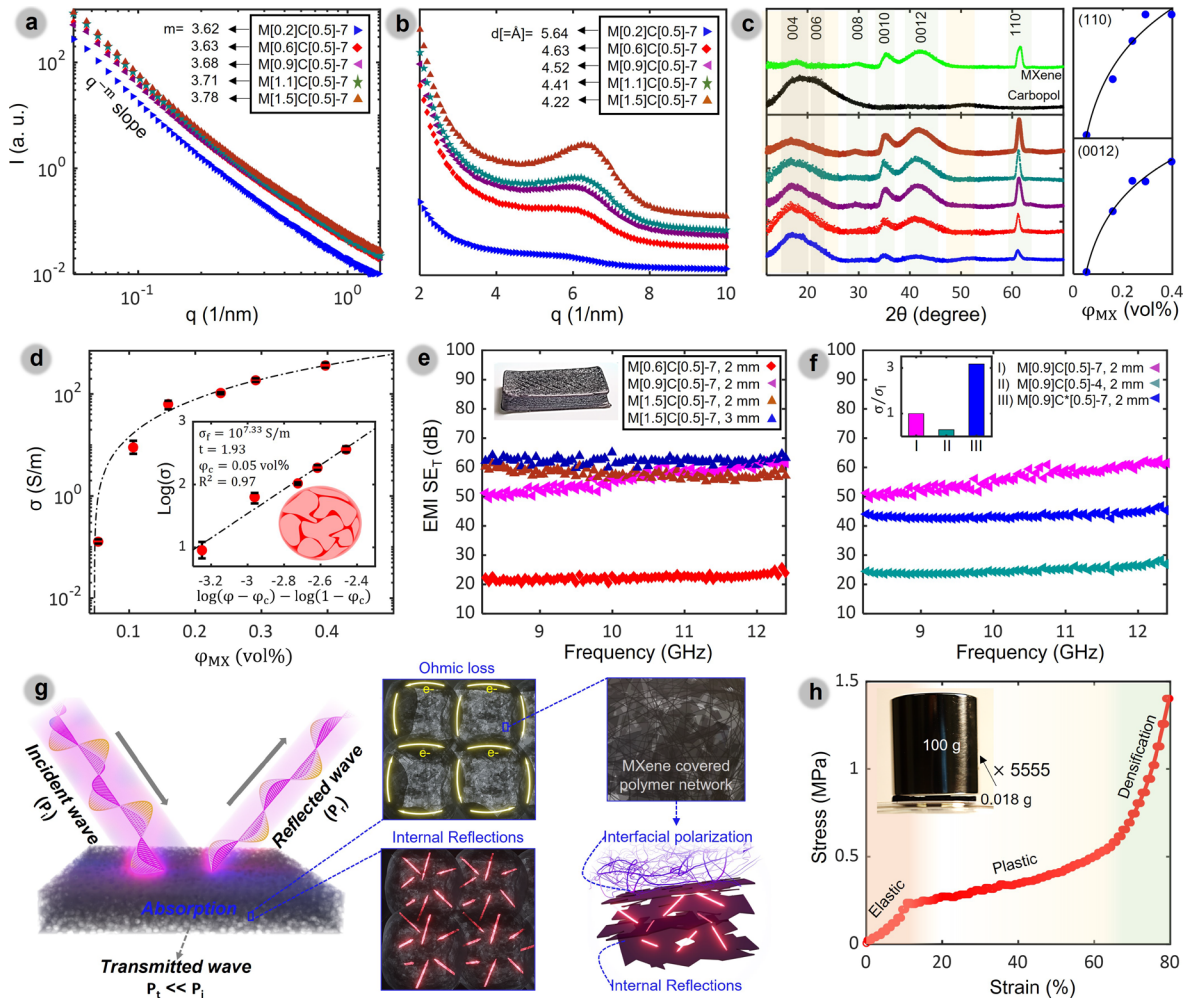

Figure 4. Solid-state structure and properties of MXene/Carbopol aerogels. (a) SAXS and (b) WAXS scattering profiles, (c) XRD patterns. (d) Change in electrical conductivity by increasing MXene volume fractions. (e) EMI shielding effectiveness of aerogels by increasing the MXene volume fractions and (f) by changing the aggregation states of Carbopol particles. (g) EMI shielding mechanisms of MXene/Carbopol aerogels. (h) Mchanical behavior of M[1.5]C[0.5]-7 aerogel under compression.

Carbopol hybrids, providing insights into optimizing parameters based on specific final applications.

The viscoelastic response of MXene/Carbopol gels provides additional understanding of the dispersion state of MXene nanosheets and their interactions with Carbopol microgels (Figures 3e and S7, SI). In the linear viscoelastic range (LVR), where strain amplitude is small compared to the strength of the bonds maintaining the microstructure, the material behaves like a homogeneously deformable gel-like or soft solid.[48] In this region, microgels are restricted to their respective "cages" undergoing elastic deformation without significant relative movement.[37] It is hypothesized that favorable interactions between MXene and Carbopol permit nanosheets to settle on the microgel surfaces, which results in an increase in the elastic modulus in the LVR with an increase in the MXene content.

The yield point is the strain amplitude (γ_y) where reversible elastic deformation ends and irreversible deformation, or bond-breaking process, begins (Figure 3f).[48] Yielding region of MXene/Carbopol gel inks is characterized by the dominance of G' and a simultaneous overshoot in the loss modulus (Figure S7, SI). This is due to the continuous and spatially heterogeneous transition from recoverable to unrecoverable strain acquisition, which intensifies throughout the material as the deformation amplitude increases.[49,50] The nonlinear region commences beyond the crossover point of G' and G'' known as the flow point (γ_f), where dissipation predominates due to unrecoverable plastic flow[45] (Figure 3f). The high strain amplitudes in this region cause a massive bond breakage, so the microstructure is no longer percolated, and the material shows liquidlike behavior.

Up to 0.24 vol % (0.9 wt %) of MXene, γ_y and γ_f, respectively, rise from 10 and 170% for the Carbopol dispersion to 32.7 and 347% for M[0.9]-C[0.5]-7 (Figure 3g). This suggests that MXene nanosheets partially covering the microgels form a highly elastic, well-packed assembly, delaying the gel's transition to a viscoelastic and liquidlike behavior. However, with further MXene content increase to 0.4 vol % (1.5 wt %), both yield and flow points decrease to strain amplitudes of 24 and 230%, respectively. Similar to Carbopol dispersions with added spherical fillers,[51] in the MXene/Carbopol system, increasing the MXene volume percentage from 0.2 to 0.4 weakens the microgel interconnection and increases the MXene/MXene repulsive interactions. This enhances plastic deformation mechanisms and shifts the structure to viscoelastic and liquidlike regions at lower strain amplitudes. Meanwhile, the flow transition index (γ_f/γ_y), which

https://doi.org/10.1021/acsami.4c19700
ACS Appl. Mater. Interfaces 2025, 17, 4022−4032

characterizes the inner structure's breaking behavior,[52] continually decreases from 17 to 10 as the MXene content increases to 1.5 wt % (Figure 3h). This trend indicates a transition from a weak network to a stiff or brittle soft material, evidencing the structure's ability to yield, break down, and rebuild during the printing process.

To supplement the structural characterization offered by rheology, SAXS measurements are carried out on MXene/Carbopol gel inks (Figure 3i,j). It is important to note that the scattering pattern observed in SAXS is primarily due to the presence of MXene nanosheets, which have high contrast with water, while the pristine Carbopol dispersion does not exhibit any diffusive scattering pattern (Figure S8a, SI). Therefore, the structural ordering observed for hybrid systems is solely assigned to the arrangements of the MXene nanosheets.

The slope of the SAXS scattering intensity profile at very low q values can be used to determine the fractal dimensionality of the dispersed objects in the system.[53,54] The X-ray scattering intensity (I) decreases monotonically with the scattering vector modulus (q) for MXene concentrations ranging from 0.2 to 1.5 wt %, with $I \sim q^{-2}$. This follows the typical scattering law of 2D planar colloids and indicates the excellent dispersion of MXene nanosheets in gel inks (Figure 3i).

The 2D scattering pattern of the M[1.5]C[0.5]-7 gel ink shows an isotropic diffusive pattern, contrasting with the long-range orientation observed in the M[1.5] suspension (Figures 3i and S8a, SI). This confirms the confinement of MXene nanosheets between Carbopol microgels, preventing them from achieving long-range orientation.

To better illustrate the characteristic peaks related to the ordering of MXene nanosheets, the intensity is normalized by multiplication with q^2 (Figure 3j). The scattering profiles of MXene/Carbopol gel inks display notable peaks indicative of the correlation distances between the MXene nanosheets. These peaks are not observed in either MXene or Carbopol dispersions (Figure S8b, SI). Interestingly, within the studied concentration range, while the intensity of the peaks increases with MXene concentration, the correlation distances between the MXene nanosheets remain unchanged. The peaks observed in the scattering profiles at $q^*-5q^*-10q^*$ cannot be simply attributed to the lamellar ordering typically seen in suspensions of repulsive nanosheets.[54] In the MXene/Carbopol system, not only are MXene nanosheets confined between the jammed Carbopol microgels, but there are also hydrogen bonding and electrostatic repulsions between various entities such as MXene/MXene, MXene/Carbopol particles, and MXene/PAA dangling chains. To understand the ordering geometry of MXene nanosheets, future theoretical studies and computer simulations are required.

3.4. Morphology and Properties of MXene/Carbopol Aerogels. The X-ray scattering analysis (SAXS/WAXS/XRD) of aerogels in different length scales of 0.1 to 120 nm was carried out to assess the dispersion state of MXenes, as shown in Figure 4a–c. After the hydrogels were freeze-dried, the decay slope of the SAXS profile rises to 3.6–3.8 depending on the MXene concentration (Figure 4a). This suggests the restacking of MXene nanosheets after freeze-drying as a result of the high local concentration of MXenes in the confined volume between polymer agglomerates and/or creasing of nanosheets dispersed in the repulsive polymer matrix. Also, as the MXene content increases from 28 to 74 wt %, the interlayer spacing of MXene nanosheets shrinks from 5.64 to 4.22 Å, with a corresponding increase in the intensity of (002) peaks, especially above the percolation threshold (Figure 4b). This signifies enhanced face-to-face MXene assembly by increasing the MXene concentration, thus corroborating the SAXS results. This MXene assembly results in aerogels that possess both effective electrical conduction and suitable mechanical properties.

X-ray diffraction patterns at smaller length scales show the higher order (00l) peaks and (110) peak as characteristics of c-lattice and a-lattice parameters of MXenes, respectively (Figure 4c). A major peak ranging from 2θ of 10° to 25°, linked to Carbopol, is observed in aerogels' patterns, with the highest intensity measured for the aerogel containing the lowest MXene concentration (M[0.2]C[0.5]-7). On the other hand, the intensity of the (110) peak, indicating the in-plane crystalline order of MXene nanosheets, amplifies as the MXene concentration increases. High-order (00l) MXene peaks are clearly observed in the aerogels' patterns, particularly in the system with the highest degree of face-to-face MXene assembly (M[1.5]C[0.5]-7). The comparison of the intensities of MXene's characteristic peaks reveals that percolated MXene assembly occurs above 0.05 vol % MXene (Figure 4c). This structural development directly impacts the solid-state electronic properties of the MXene/Carbopol aerogels.

The effective face-to-face contact between MXene nanosheets, facilitated by the closely packed segregated morphology of the MXene/Carbopol system, results in excellent electrical conductivity of approximately 360 S·m^{-1}, even at low MXene concentrations of only 0.4 vol %. (Figure 4d). This is why the electrical conductivity of the MXene/Carbopol aerogel greatly exceeds that of other segregated structures prepared using spherical polymer particles as templates (Table S4, SI). As suggested by the X-ray diffraction patterns, a rapid increase in direct electrical conductivity is observed at 0.05 vol % MXene, with a conductivity of 0.15 S·m^{-1}, which greatly surpasses the antistatic criterion (10^{-6} S·m^{-1}).[49] Increasing MXene loading above 0.11 vol % yields a more gradual rise in electrical conductivity, e.g., ≈63 and 104 S·m^{-1} at 0.16 and 0.23 vol %, respectively. This enhancement in electrical conductivity exemplifies the formation of interconnected conductive paths between MXene nanosheets and can be described by the bond percolation model. Above the percolation threshold, the bond percolation model offers a power law, $\sigma_c = \sigma_{MX}[(\varphi - \varphi_c)/(1 - \varphi_c)]^t$, for the conductivity of the composite, where "σ_{MX}" represents conductivity of the MXene, "φ" is the filler volume fraction, "φ_c" is the percolation threshold, and "t" is the so-called universal critical exponent. In the MXene/Carbopol system, the critical exponent "t" is 1.93, which is close to the theoretical universal value of 2 for 3D systems.[55] The electrical percolation in the solid state (0.05 vol %) precedes the rheological percolation (0.1 vol %) of MXene/Carbopol gel inks. This is attributed to the proximity of MXene nanosheets after the removal of interlayer water molecules, which facilitate electron hopping between nanosheets.

The EMI shielding effectiveness (SE) of aerogels that contain a well-developed electrically conductive network of MXene nanosheets was evaluated (Figures 4e,f, S10, SI and eqs S1–S3, SI). The physical properties of the tested aerogels, which were prepared via 3D printing, are presented in Table S5 and Figure S9, SI. When the MXene concentration increases from 53 to 63 wt %, SE_T increases from 22.5 to 57 dB (Figure 4e). However, a further increase in the MXene concentration to 74 wt % only improves the shielding effectiveness by about 3 dB. This suggests that a well-developed, space-spanning

https://doi.org/10.1021/acsami.4c19700
ACS Appl. Mater. Interfaces 2025, 17, 4022–4032

MXene network is formed at only 63 wt % (0.24 vol %) of MXene, which can shield more than 99% of incident EM waves.

Moreover, for the M[1.5]C[0.5]-7 sample with the highest MXene content, there is no significant change in the shielding effectiveness when the thickness of the shield is increased from 2 to 3 mm. This negligible effect of material thickness on the shielding effectiveness is attributed to the decreased attenuation constant for highly porous materials, a phenomenon also observed in other systems.[56]

Figure 4f compares the shielding effectiveness of aerogels with a consistent MXene content of 53 wt % but with varying dispersion states of MXene and Carbopol (Figure S10, SI). The aggregation of MXene nanosheets at a low pH (in the M[0.9]C[0.5]-4 system) reduces the electrical conductivity by 3 times compared to the system with a homogeneous MXene distribution (inset of Figure 4f). Consequently, the non-homogenous system shows a minimum shielding effectiveness of about 24 dB.

On the other hand, increasing the cross-link density of Carbopol particles leads to a larger cell size for the aerogel and reduces the accessible volume for displacing MXene nanosheets. This corresponds to a higher density of MXene nanosheets in cell walls and thereby enhances interconnections between the nanosheets, improving electron conduction in M[0.9]C*[0.5]-7 system (Figure 4f). In contrast, the shielding effectiveness drops to approximately 42 dB due to the system's reduced absorption capability through interfacial polarization at MXene/polymer interfaces and/or internal reflections in the aerogel with a larger cell size (Figure 4g).

These results clearly demonstrate the interplay between electrical conductivity and porous morphology in the attenuation of electromagnetic waves. It is important to note, however, that the impact of porous morphology on the shielding effectiveness may differ depending on the electrical conductivity of the MXene assemblies, and varying trends may be observed in different situations.[7,52] The manipulation of the dispersion state of MXene nanosheets and Carbopol particles optimizes the processability of MXene/Carbopol gel inks, ultimately refining the electric and electromagnetic properties of the resulting aerogels. The MXene/Carbopol aerogels exhibit comparable performance to other aerogels prepared using the template method (as shown in Table S4, SI); however, the MXene/Carbopol aerogel stands out because of its compatibility with 3D printing processes and its simultaneous high electrical conductivity and EMI shielding effectiveness, even at the low thickness and solid content.

MXene/Carbopol aerogel exhibits the characteristic mechanical response of foamlike materials with three distinct regions: elastic, plateau (plastic), and densification (Figure 4h). The MXene nanosheets are the main component of the cell walls in the M[1.5]C[0.5]-7 aerogel, contributing to an elastic modulus of 1.75 MPa, an elastic yield stress of 250 kPa, and a compression strength of about 1.4 MPa. Interestingly, the aerogel can support more than 5000 times its own weight without collapsing due to its impressive elastic modulus at a mere mass of 18 mg. This robustness indicates the broad application potential of the MXene/Carbopol aerogel across diverse fields. Beyond a deformation of 65%, the densification region begins, which corresponds to a state in which the majority of cells are damaged due to the substantial load, causing the cell walls to come in contact with one another. The structure after load removal is not recoverable due to the minimum elastic properties of Carbopol in its solid state and/or the inherent brittleness of the MXene cell walls. However, the swelling of Carbopol particles can act as a stimulus, restoring the collapsed cells to their original arrangements within the material (Video S1, SI). When compared to previously reported MXene/polymer foams, the elastic modulus and compression strength of the MXene/Carbopol aerogel are notably superior (Table S6, SI).

4. CONCLUSIONS

This study introduces a novel approach to designing a 3D-printable MXene ink with optimized rheological and mechanical properties, leveraging the unique jamming effects of Carbopol microgels to guide the MXene nanosheet assembly. By serving as templates, the jammed Carbopol microgels create a percolated, densely packed network of MXene nanosheets with minimal solid content (2 wt %), achieving a viscosity of 50,000 Pa·s and a yield stress up to 400 Pa. This synergy between jamming and percolation results in a viscoelastic ink, facilitating high-precision extrusion printing and enabling the creation of free-standing 3D structures with excellent shape fidelity and stability. The encapsulation of Carbopol microgels within an MXene network provides the resulting aerogels, after freeze-drying, with a highly porous yet mechanically robust structure, boasting over 98% porosity. This structure supports a lightweight, conductive MXene network that demonstrates superior EM shielding efficiency of 57 dB at an ultralow density of 25 mg/cm^3. These properties align the MXene/Carbopol aerogels with the characteristics of *mechanical metamaterials*, where disorder and jamming yield unique structural advantages, including a high compressive modulus and EMI shielding performance.

The high conductivity and durability of the MXene/Carbopol aerogels make them promising candidates for advanced applications across multiple fields, including energy storage and wearable and implantable electronics. By applying principles of jamming and synergistic network formation, this method extends beyond MXene-based systems and offers a versatile platform for developing printable inks with other 2D nanomaterials. In doing so, it opens a pathway toward the scalable fabrication of lightweight, high-performance materials, aligning with the evolving needs of smart device technologies and EMI shielding applications in advanced metamaterials.

■ ASSOCIATED CONTENT

Supporting Information

The Supporting Information is available free of charge at https://pubs.acs.org/doi/10.1021/acsami.4c19700.

SEM image of MAX particles and MXene nanosheets and size distribution of MXene nanosheets from SEM images and DLS data; XRD patterns of MAX and MXene powders; optical image of MXene/Carbopol gel ink postcentrifugation; nitrogen adsorption/desorption spectra and EDS mapping of M[1.5]C[0.5]-7 aerogel; SAXS intensity profiles of pristine MXene suspensions; size distributions of MXenes with small flake sizes; rheology of gel inks under oscillation amplitude sweep; SAXS intensity profiles of MXene suspension, Carbopol dispersion, and M[1.5]C[0.5]-7 gel; TGA curve of MXene, Carbopol, and M[1.5]C[0.5]-7 hybrid; transmission, absorption, and reflection loss of MXene/Carbopol aerogels; composition details of MXene/

https://doi.org/10.1021/acsami.4c19700
ACS Appl. Mater. Interfaces 2025, 17, 4022−4032

Carbopol samples; Herschel−Bulkley model fitted parameters of gel inks; rheological properties of MXene/Carbopol gel ink compared to other MXene-based inks; electrical properties of MXene/Carbopol gel ink compared to other template-assisted assemblies; physical properties of MXene/Carbopol aerogels used for EMI shielding tests; and compression mechanical properties of MXene/Carbopol foams compared to others (PDF)

Structural restoration of the compressed hybrid aerogel by rehydration (MP4)

AUTHOR INFORMATION

Corresponding Author

Nader Taheri-Qazvini − *Department of Chemical Engineering and Department of Biomedical Engineering, University of South Carolina, Columbia, South Carolina 29208, United States;* orcid.org/0000-0003-2114-7338; Email: ntaheri@cec.sc.edu

Authors

Farivash Gholamirad − *Department of Chemical Engineering, University of South Carolina, Columbia, South Carolina 29208, United States;* orcid.org/0000-0001-7097-1353

Monirosadat Sadati − *Department of Chemical Engineering, University of South Carolina, Columbia, South Carolina 29208, United States;* orcid.org/0000-0001-9701-9637

Complete contact information is available at: https://pubs.acs.org/10.1021/acsami.4c19700

Author Contributions

F.G.: Conceptualization, methodology, investigation, validation, visualization, and writing-original draft. M.S.: Resources and writing-review and editing. N.T.Q.: Supervision, funding acquisition, conceptualization, and writing-review and editing. All authors have approved the final version of the manuscript.

Notes

The authors declare no competing financial interest.

ACKNOWLEDGMENTS

This research was supported by funding from the National Science Foundation, USA (award # 2238908) and a SPARC graduate research grant from the office of the vice president for research at the University of South Carolina. We appreciate Prof. G. Wang from the Electrical Engineering Department at the University of South Carolina for providing access to the vector network analyzer.

REFERENCES

(1) Wanasinghe, D.; Aslani, F. A review on recent advancement of electromagnetic interference shielding novel metallic materials and processes. *Composites Part B: Engineering* **2019**, *176*, No. 107207.

(2) Chung, D. D. L. Materials for electromagnetic interference shielding. *Mater. Chem. Phys.* **2020**, *255*, No. 123587.

(3) Pandey, R.; Tekumalla, S.; Gupta, M. *EMI shielding of metals, alloys, and composites*; Elsevier, 2020; pp 341−355.

(4) Liu, J.; Yu, M.-Y.; Yu, Z.-Z.; Nicolosi, V. Design and advanced manufacturing of electromagnetic interference shielding materials. *Mater. Today* **2023**, *66*, 245−272.

(5) Sawant, K. K.; Satapathy, A.; Mahimkar, K.; Krishnamurthy, S.; Kaur, A.; Kandasubramanian, B.; Raj, A. A. B. Recent Advances in MXene Nanocomposites as Electromagnetic Radiation Absorbing Materials. *J. Electron. Mater.* **2023**, *52* (6), 3576−3590.

(6) Verma, R.; Thakur, P.; Chauhan, A.; Jasrotia, R.; Thakur, A. A review on MXene and its' composites for electromagnetic interference (EMI) shielding applications. *Carbon* **2023**, *208*, 170−190.

(7) Gholamirad, F.; Ge, J.; Sadati, M.; Wang, G.; Taheri-Qazvini, N. Tuning the Self-Assembled Morphology of Ti3C2Tx MXene-Based Hybrids for High-Performance Electromagnetic Interference Shielding. *ACS Appl. Mater. Interfaces* **2022**, *14*, 49158.

(8) Jia, F.; Dong, J.; Dai, X.; Liu, Y.; Wang, H.; Lu, Z. Robust, flexible, and stable CuNWs/MXene/ANFs hybrid film constructed by structural assemble strategy for efficient EMI shielding. *Chemical Engineering Journal* **2023**, *452* (P2), No. 139395.

(9) Li, Q.; Sun, Y.; Zhou, B.; Han, G.; Feng, Y.; Liu, C.; Shen, C. Flexible, Stretchable, and Transparent MXene Nanosheet/Thermoplastic Polyurethane Films for Multifunctional Heating and Electromagnetic Interference Shielding. *ACS Applied Nano Materials* **2023**, *6* (5), 3395−3404.

(10) Zhang, Y.; Gao, Q.; Sheng, X.; Zhang, S.; Chen, J.; Ma, Y.; Qin, J.; Zhao, Y.; Shi, X.; Zhang, G. Flexible, robust, sandwich structure polyimide composite film with alternative MXene and Ag NWs layers for electromagnetic interference shielding. *Journal of Materials Science & Technology* **2023**, *159*, 194−203.

(11) Zhuo, L.; Cai, Y.; Shen, D.; Gou, P.; Wang, M.; Hu, G.; Xie, F. Anti-oxidation polyimide-based hybrid foams assembled with bilayer coatings for efficient electromagnetic interference shielding. *Chemical Engineering Journal* **2023**, *451* (P3), No. 138808.

(12) Lu, Y.; Zhao, X.; Lin, Y.; Li, P.; Tao, Y.; Wang, Z.; Ma, J.; Xu, H.; Liu, Y. Lightweight MXene/carbon composite foam with hollow skeleton for air-stable, high-temperature-resistant and compressible electromagnetic interference shielding. *Carbon* **2023**, *206*, 375−382.

(13) Gholamirad, F.; Taheri-Qazvini, N. Three-Dimensional Porous $Ti_3C_2T_x$ MXene-Based Hybrids Formed by Charge-Driven Assembly. *Chem. Mater.* **2021**, *33* (24), 9560−9570.

(14) Li, Z.; Sun, Y.; Zhou, B.; Feng, Y.; Liu, C.; Shen, C. Flexible thermoplastic polyurethane/MXene foams for compressible electromagnetic interference shielding. *Materials Today Physics* **2023**, *32*, No. 101017.

(15) Zhang, C.; McKeon, L.; Kremer, M. P.; Park, S.-H.; Ronan, O.; Seral-Ascaso, A.; Barwich, S.; Coileáin, C. Ó.; McEvoy, N.; Nerl, H. C.; et al. Additive-free MXene inks and direct printing of micro-supercapacitors. *Nat. Commun.* **2019**, *10* (1), 1795−1795.

(16) Saadi, M. A. S. R.; Maguire, A.; Pottackal, N. T.; Thakur, M. S. H.; Ikram, M. M.; Hart, A. J.; Ajayan, P. M.; Rahman, M. M. Direct Ink Writing: A 3D Printing Technology for Diverse Materials. *Adv. Mater.* **2022**, *34* (28), 2108855−2108855.

(17) Orangi, J.; Hamade, F.; Davis, V. A.; Beidaghi, M. 3D Printing of Additive-Free 2D $Ti_3C_2T_x$ (MXene) Ink for Fabrication of Micro-Supercapacitors with Ultra-High Energy Densities. *ACS Nano* **2020**, *14* (1), 640−650.

(18) Yuan, M.; Wang, L.; Liu, X.; Du, X.; Zhang, G.; Chang, Y.; Xia, Q.; Hu, Q.; Zhou, A. 3D printing quasi-solid-state micro-supercapacitors with ultrahigh areal energy density based on high concentration MXene sediment. *Chemical Engineering Journal* **2023**, *451*, No. 138686.

(19) Chen, D.; Long, Y.; Wu, Z.; Dong, X.; Wang, N.; Yu, J.; Han, D.; Tao, Y.; Yang, Q. H. A Gelation-Assisted Approach for Versatile MXene Inks. *Adv. Funct. Mater.* **2022**, *32*, No. 2204372.

(20) Ghaffarkhah, A.; Kamkar, M.; Dijvejin, Z. A.; Riazi, H.; Ghaderi, S.; Golovin, K.; Soroush, M.; Arjmand, M. High-resolution extrusion printing of Ti_3C_2-based inks for wearable human motion monitoring and electromagnetic interference shielding. *Carbon* **2022**, *191*, 277−289.

(21) Hua, T.; Guo, H.; Qin, J.; Wu, Q.; Li, L.; Qian, B. 3D printing lamellar $Ti_3C_2T_x$ MXene/graphene hybrid aerogels for enhanced electromagnetic interference shielding performance. *RSC Adv.* **2022**, *12* (38), 24980−24987.

(22) Qi, C.-Z.; Wu, X.; Liu, J.; Luo, X.-J.; Zhang, H.-B.; Yu, Z.-Z. Highly conductive calcium ion-reinforced MXene/sodium alginate aerogel meshes by direct ink writing for electromagnetic interference

shielding and Joule heating. *Journal of Materials Science & Technology* **2023**, *135*, 213−220.
(23) Shao, Y.; Wei, L.; Wu, X.; Jiang, C.; Yao, Y.; Peng, B.; Chen, H.; Huangfu, J.; Ying, Y.; Zhang, C. J.; et al. Room-temperature high-precision printing of flexible wireless electronics based on MXene inks. *Nat. Commun.* **2022**, *13* (1), 3223−3223.
(24) Shi, G.; Zhu, Y.; Batmunkh, M.; Ingram, M.; Huang, Y.; Chen, Z.; Wei, Y.; Zhong, L.; Peng, X.; Zhong, Y. L. Cytomembrane-Inspired MXene Ink with Amphiphilic Surfactant for 3D Printed Microsupercapacitors. *ACS Nano* **2022**, *16* (9), 14723−14736.
(25) Wu, X.; Tu, T.; Dai, Y.; Tang, P.; Zhang, Y.; Deng, Z.; Li, L.; Zhang, H.-B.; Yu, Z.-Z. Direct Ink Writing of Highly Conductive MXene Frames for Tunable Electromagnetic Interference Shielding and Electromagnetic Wave-Induced Thermochromism. *Nano-Micro Letters* **2021**, *13* (1), 148−148.
(26) Xue, T.; Yang, Y.; Yu, D.; Wali, Q.; Wang, Z.; Cao, X.; Fan, W.; Liu, T. 3D Printed Integrated Gradient-Conductive MXene/CNT/Polyimide Aerogel Frames for Electromagnetic Interference Shielding with Ultra-Low Reflection. *Nano-Micro Letters* **2023**, *15* (1), 45−45.
(27) Zhou, G.; Li, M. C.; Liu, C.; Wu, Q.; Mei, C. 3D Printed $Ti_3C_2T_x$ MXene/Cellulose Nanofiber Architectures for Solid-State Supercapacitors: Ink Rheology, 3D Printability, and Electrochemical Performance. *Adv. Funct. Mater.* **2022**, *32* (14), 2109593−2109593.
(28) Zou, G.; Sun, J.; Fan, Z.; Jin, J.; Li, C.; Cai, J.; Wei, C.; Shao, Y. 3D-printed zn-ion hybrid capacitor enabled by universal divalent cation-gelated additive-free Ti_3C_2 mxene ink. *ACS Nano* **2021**, *15* (2), 3098−3107.
(29) Amini, M.; Kamkar, M.; Ahmadijokani, F.; Ghaderi, S.; Rojas, O. J.; Hosseini, H.; Arjmand, M. Mapping 3D printability of ionically cross-linked cellulose nanocrystal inks: architecting from Nano-to macroscale structures. *Biomacromolecules* **2023**, *24* (2), 775−788.
(30) Kyle, S.; Jessop, Z. M.; Al-Sabah, A.; Whitaker, I. S. 'Printability' of Candidate Biomaterials for Extrusion Based 3D Printing: State-of-the-Art. *Adv. Healthcare Mater.* **2017**, *6* (16), 1−16.
(31) Liu, J.; McKeon, L.; Garcia, J.; Pinilla, S.; Barwich, S.; Möbius, M.; Stamenov, P.; Coleman, J. N.; Nicolosi, V. Additive Manufacturing of Ti_3C_2-MXene-Functionalized Conductive Polymer Hydrogels for Electromagnetic-Interference Shielding. *Adv. Mater.* **2022**, *34* (5), No. 2106253.
(32) Li, L.; Deng, Z.; Chen, M.; Yu, Z. Z.; Russell, T. P.; Zhang, H. B. 3D Printing of Ultralow-Concentration 2D Nanomaterial Inks for Multifunctional Architectures. *Nano Lett.* **2023**, *23* (1), 155−162.
(33) Liu, X.; Zheng, B.; Hua, Y.; Lu, S.; Nong, Z.; Wang, J.; Song, Y. Ultralight MXene/rGO aerogel frames with component and structure controlled electromagnetic wave absorption by direct ink writing. *Carbon* **2024**, *230*, No. 119650.
(34) Hashemi, S. A.; Ghaffarkhah, A.; Hosseini, H.; Arjmand, M. 3D-Printed Interfacially Jammed Emulsion Aerogels. *ACS Appl. Mater. Interfaces* **2024**, *16* (35), 46923−46936.
(35) Ghaffarkhah, A.; Hashemi, S. A.; Rostami, S.; Amini, M.; Ahmadijokani, F.; Pournaghshband Isfahani, A.; Mhatre, S. E.; Rojas, O. J.; Kamkar, M.; Wuttke, S. Ultra-flyweight cryogels of MXene/graphene oxide for electromagnetic interference shielding. *Adv. Funct. Mater.* **2023**, *33* (50), No. 2304748.
(36) Oelschlaeger, C.; Marten, J.; Péridont, F.; Willenbacher, N. Imaging of the microstructure of Carbopol dispersions and correlation with their macroelasticity: A micro- and macrorheological study. *J. Rheol.* **2022**, *66* (4), 749−760.
(37) Varges, P. R.; Costa, C. M.; Fonseca, B. S.; Naccache, M. F.; De Souza Mendes, P. Rheological Characterization of Carbopol® Dispersions in Water and in Water/Glycerol Solutions. *Fluids* **2019**, *4* (1), 3.
(38) Kim, J. Y.; Song, J. Y.; Lee, E. J.; Park, S. K. Rheological properties and microstructures of Carbopol gel network system. *Colloid Polym. Sci.* **2003**, *281* (7), 614−623.
(39) Jaworski, Z.; Spychaj, T.; Story, A.; Story, G. Carbomer microgels as model yield-stress fluids. *Reviews in Chemical Engineering* **2022**, *38* (7), 881−919.
(40) Ouyang, L.; Yao, R.; Zhao, Y.; Sun, W. Effect of bioink properties on printability and cell viability for 3D bioplotting of embryonic stem cells. *Biofabrication* **2016**, *8* (3), No. 035020.
(41) Li, K.; Zhao, J.; Zhussupbekova, A.; Shuck, C. E.; Hughes, L.; Dong, Y.; Barwich, S.; Vaesen, S.; Shvets, I. V.; Möbius, M.; et al. 4D printing of MXene hydrogels for high-efficiency pseudocapacitive energy storage. *Nat. Commun.* **2022**, *13* (1), 6884.
(42) Yang, W.; Yang, J.; Byun, J. J.; Moissinac, F. P.; Xu, J.; Haigh, S. J.; Domingos, M.; Bissett, M. A.; Dryfe, R. A. W.; Barg, S. 3D Printing of Freestanding MXene Architectures for Current-Collector-Free Supercapacitors. *Adv. Mater.* **2019**, *31* (37), 1902725−1902725.
(43) Yi, Q.; Pei, X.; Das, P.; Qin, H.; Lee, S. W.; Esfandyarpour, R. A Self-powered Triboelectric MXene-based 3D-printed Wearable Physiological Biosignal Sensing System for On-demand, Wireless, and Real-time Health Monitoring. *Nano Energy* **2022**, *101*, No. 107511.
(44) Zhang, J.; Uzun, S.; Seyedin, S.; Lynch, P. A.; Akuzum, B.; Wang, Z.; Qin, S.; Alhabeb, M.; Shuck, C. E.; Lei, W.; et al. Additive-Free MXene Liquid Crystals and Fibers. *ACS Central Science* **2020**, *6* (2), 254−265.
(45) Mir, S. M.; Jafari, S. H.; Khonakdar, H. A.; Krause, B.; Pötschke, P.; Taheri Qazvini, N. A promising approach to low electrical percolation threshold in PMMA nanocomposites by using MWCNT-PEO predispersions. *Materials and Design* **2016**, *111*, 253−262.
(46) Chen, X.; Yang, R.; Wu, X. Printing of MXene-based materials and the applications: a state-of-the-art review. *2D Materials* **2022**, *9* (4), No. 042002.
(47) Shayesteh Zeraati, A.; Mirkhani, S. A.; Sun, P.; Naguib, M.; Braun, P. V.; Sundararaj, U. Improved synthesis of Ti3C2T: XMXenes resulting in exceptional electrical conductivity, high synthesis yield, and enhanced capacitance. *Nanoscale* **2021**, *13* (6), 3572−3580.
(48) Mezger, T. The Rheology Handbook. *Vincentz Network* **2020**.
(49) Donley, G. J.; Singh, P. K.; Shetty, A.; Rogers, S. A. Elucidating the G″ overshoot in soft materials with a yield transition via a time-resolved experimental strain decomposition. *Proc. Natl. Acad. Sci. U. S. A.* **2020**, *117* (36), 21945−21952.
(50) Kamani, K.; Donley, G. J.; Rogers, S. A. Unification of the Rheological Physics of Yield Stress Fluids. *Phys. Rev. Lett.* **2021**, *126* (21), No. 218002.
(51) Baek, G.; Kim, C. Rheological properties of Carbopol containing nanoparticles. *J. Rheol.* **2011**, *55* (2), 313−330.
(52) Corker, A.; Ng, H. C. H.; Poole, R. J.; García-Tuñón, E. 3D printing with 2D colloids: designing rheology protocols to predict 'printability' of soft-materials. *Soft Matter* **2019**, *15* (6), 1444−1456.
(53) Nassira, H.; Sánchez-Ferrer, A.; Adamcik, J.; Handschin, S.; Mahdavi, H.; Taheri Qazvini, N.; Mezzenga, R. Gelatin−Graphene Nanocomposites with Ultralow Electrical Percolation Threshold. *Adv. Mater.* **2016**, *28*, 6914−6920.
(54) Xu, Z.; Gao, C. Graphene chiral liquid crystals and macroscopic assembled fibres. *Nat. Commun.* **2011**, *2* (1), 571−571.
(55) Stauffer, D.; Aharony, A. *Introduction To Percolation Theory*; Taylor & Francis, 2018.
(56) Ma, L.; Hamidinejad, M.; Wei, L.; Zhao, B.; Park, C. B. Absorption-dominant EMI shielding polymer composite foams: Microstructure and geometry optimization. *Materials Today Physics* **2023**, *30*, No. 100940.

https://doi.org/10.1021/acsami.4c19700
ACS Appl. Mater. Interfaces 2025, 17, 4022−4032